J. Fluid Mech. (2022), *vol*. 952, R3, doi:10.1017/jfm.2022.901

Modelling falling film flow: an adjustable formulation

Sanghasri Mukhopadhyay[1], **Christian Ruyer-Quil**[2],† **and R. Usha**[3]

[1]Department of Mathematics, School of Advanced Science, Vellore Institute of Technology, Vellore 632014, Tamil Nadu, India

[2]Université Savoie Mont Blanc, CNRS, LOCIE, 73000 Chambéry, France

[3]Department of Mathematics, IIT Madras, Chennai 600036, Tamil Nadu, India

(Received 23 June 2022; revised 21 October 2022; accepted 24 October 2022)

A new two-equation model for gravity-driven liquid film flow based on the long-wave expansion has been derived. The novelty of the model consists in using a base velocity profile combining parabolic (Ruyer-Quil & Manneville, *Eur. Phys. J.* B, vol. 15, issue 2, 2000, pp. 357–369) and ellipse (Usha *et al.*, *Phys. Fluids*, vol. 32, issue 1, 2020, 013603) profile functions in the wall-normal coordinate. The dependence on a free parameter A related to the eccentricity of an ellipse serves as an adjustable parameter. The resulting models are consistent at $O(\varepsilon)$ for inertia terms and at $O(\varepsilon^2)$ for viscous diffusion effects, and predict accurately the primary instability. Appropriate tuning of the adjustable parameter helps to recover accurate predictions for the asymptotic wave celerity of nonlinear solitary waves. Further, the model is shown to capture the closed separation vortices that can form underneath the troughs of precursory capillary ripples.

Key words: thin films, low-dimensional models, solitary waves

1. Introduction

A long-standing challenge in falling film flows has been to develop simple and accurate models that capture their nonlinear wavy dynamics. There have been continued efforts by researchers to optimise the chemical engineering processes that involve these flows and obtain models that are based on the fundamental closure assumption for the streamwise velocity distribution – see the reviews by Kalliadasis *et al.* (2012), Noble & Vila (2013), Ruyer-Quil *et al.* (2014), Richard, Ruyer-Quil & Vila (2016) and Richard *et al.* (2019) for recent attempts. To the best of our knowledge, the four-equation model derived by Ruyer-Quil & Manneville (2000) using a weighted residual method (WRM) is the

† Email address for correspondence: Christian.Ruyer-Quil@univ-smb.fr

© The Author(s), 2022. Published by Cambridge University Press

https://doi.org/10.1017/jfm.2022.901 Published online by Cambridge University Press

most accurate. This model precisely captures the characteristics of the solitary waves that dominate and organise the noise-driven dynamics of falling films. Although the four-equation WRM model is fully consistent at second order, its complicated expression hampers its use in the film flow community. This inspired the development and wide use of a simplified two-equation WRM model, in spite of its moderate overestimation of the velocity of solitary waves. This two-equation model is hereinafter referred to as the Ruyer-Quil and Manneville (RQM) model.

In fact, two-equation models, which can be viewed as extensions to viscous flows of the Saint-Venant formalism of shallow-water flows, offer the most promising framework. This motivated Richard *et al.* (2019) to consider all consistent two-equation models that can be derived by in-depth integration of the momentum balance (momentum integral method or MIM) or by integration of the energy balance (energy integral method or EIM). They showed that it is possible to derive consistent two-equation models up to first order for inertia terms and second-order for viscous diffusion which present optimal mathematical properties (conservation equations preserving mathematical entropy). Although some formulations of two-equation models could accurately predict the asymptotic speed of solitary waves, none of them turned out to be fully satisfactory. In particular, reconstruction of the velocity field from this approach poses difficulty, as the derivation of these models is based on the asymptotics of the velocity. In principle, predictions of the flow field under the waves are thus limited to only small-amplitude waves and low values of the Reynolds number, where the long-wave expansion is strictly valid.

Conversely, Ruyer-Quil & Manneville (2002) have shown that any WRM converges to a unique expression of the WRM models if the number of test functions is sufficient. In fact, the expressions of these models are entirely determined by the ansatz for the velocity profile across the film or closure hypothesis (Ruyer-Quil *et al.* 2014). This raises the question of the quest for an educated guess for the velocity, yielding the best two-equation model within the WRM. This approach has the advantage to provide unambiguous information on the velocity field under the waves.

Recently, Usha, Chattopadhyay & Tiwari (2020) have proposed an ellipse profile for the velocity field and derived a new first-order model by employing the EIM. The choice of ellipse profile as weight function in that study was motivated by the success of the EIM with an ellipse profile in accurately and effectively predicting the squeeze film force in squeeze flow problems and in predicting the inertial effects on the performance of squeeze film dampers (Han & Rogers 1996). This choice allows for a free parameter in the velocity profile, which is related to the eccentricity of the ellipse, and this helps in adjusting the profile. The results reveal that, as this free parameter is increased but remains finite, there is significant improvement in the predictions in the inertia-dominant regimes.

In this paper, we introduce an adjustable velocity profile based on the elliptic profile and investigate how the eccentricity of this profile influences the properties of the resulting WRM models. A variant of the ellipse profile (see § 2) is employed for the velocity distribution, yielding a two-equation model with an adjustable parameter, which is referred to as the ellipse velocity profile (EVP) model. The EVP model, though consistent at first order for inertia and at second order for viscous terms, does not present the expected structure of a shallow-water model, where convective terms are quadratic with respect to the velocity (or flow rate q) and diffusion terms are linear with respect to q. A modified model (EVPM) having this structure is proposed instead. As a first step in assessing the performance of the derived models, the characteristics of single-hump solitary wave

https://doi.org/10.1017/jfm.2022.901 Published online by Cambridge University Press

solutions are obtained and are compared with the characteristics of the direct numerical simulation (DNS) of the Navier–Stokes equations presented by Chakraborty *et al.* (2014).

2. Mathematical modelling

We consider a liquid film flowing down a plane making an angle β with the horizontal. The fluid properties, i.e. kinematic viscosity $\nu = \mu/\rho$, density ρ and surface tension σ, are constant. At the free surface, the gas is considered to be passive, with a constant pressure. We assume a slow evolution of the liquid film in space and time and introduce a film parameter ε as a formal parameter, which is inserted along with each derivative ∂_x and ∂_t in space and time. This allows us to apply Prandtl's simplification of the cross-stream momentum balance, which gives

$$\varepsilon\delta(u_t + uu_x + vu_y) = b(h) + u_{yy} + \varepsilon^2\eta(2u_{xx} + [u_x|_{y=h}]_x), \tag{2.1a}$$

$$u_x + v_y = 0, \quad u|_{y=0} = v|_{y=0}, \tag{2.1b}$$

$$u_y|_{y=h} = \varepsilon^2\eta(4h_x u_x|_{y=h} - v_x|_{y=h}), \quad v|_{y=h} = h_t + u|_{y=h}h_x. \tag{2.1c}$$

Here $b(h) = 1 - \varepsilon\zeta h_x + \varepsilon^3 h_{xxx}$ combines the streamwise gravity acceleration (body force) and a pressure gradient with a hydrostatic part and a contribution of surface tension.

System (2.1) is obtained after elimination of the pressure field and is consistent up to $O(\varepsilon^2)$ (Ruyer-Quil & Manneville 2000). We chose to write (2.1) using Shkadov's notation, for which the time t and the streamwise coordinate x have been compressed by a ratio $\kappa = (l_c/h_N)^{2/3}$, where $l_c = \sqrt{\sigma/(\rho g \sin(\beta))}$ is a capillary length and h_N is the thickness of the uniform film (Nusselt solution). The spatial coordinates x and y have been made dimensionless with the scales κh_N and h_N, respectively. The time scale is $\kappa h_N/u_N$, where $u_N = g\sin(\beta)h_N^2/\nu$ is three times the averaged speed of the Nusselt solution, which corresponds to the speed of kinematic waves at the free surface in the very-long-wave limit. Similarly, the velocity components u and v have been made dimensionless with the scales u_N and u_N/κ, respectively. This choice of scales enables us to limit significantly the number of coefficients in (2.1) differing from unity. In particular, κ is adjusted so that the surface tension term bears a coefficient equal to one.

Three dimensionless groups characterise the flow: the reduced Reynolds number $\delta = 3Re/\kappa$, where $Re = u_N h_N/(3\nu)$ is the Reynolds number based on the averaged velocity $u_N/3$; a reduced slope $\zeta = \cot(\beta)/\kappa$; and a parameter $\eta = 1/\kappa^2$ that compares viscous diffusion and capillary damping of the waves. The reduced Reynolds number δ compares inertia and viscosity at a scale where surface tension is dominant. Ooshida (1999) showed that δ discriminates between two different regimes for which travelling waves present different tail lengths and properties, which he called the 'drag–gravity' and 'drag–inertia' regimes. Finally, we introduce the Kapitza number $Ka = \sigma/(\rho\nu^{4/3}g^{1/3})$, which compares surface tension, viscosity and gravity. This parameter depends only on the fluid properties.

The Nusselt flat-film flow solution can be written as

$$u = h^2\left(\frac{y}{h} - \frac{1}{2}\frac{y^2}{h^2}\right) \equiv h^2 g_0(\bar{y}), \quad \text{where } \bar{y} = y/h. \tag{2.2}$$

The velocity is then parametrised with only one field, namely the film thickness h, which is also the amplitude of the long-wave surface mode of instability. Yet, the velocity distribution of large-amplitude waves may significantly depart from the Nusselt solution. This is an effect of the inertia of the film. An easy way to account for this effect is to

https://doi.org/10.1017/jfm.2022.901 Published online by Cambridge University Press

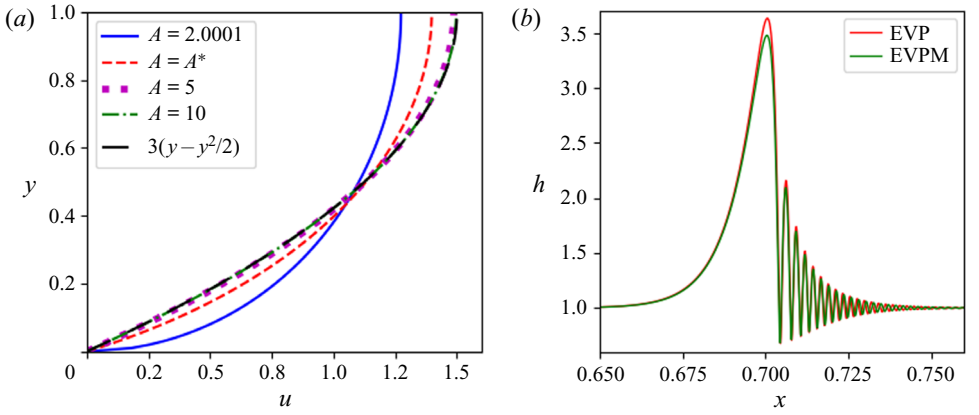

Figure 1. (*a*) Base flow for different values of A. (*b*) Solitary wave profiles corresponding to solutions to EVP and EVPM models (2.8) and (2.9) for $\theta = 90$, $Ka = 3400$, $\delta = 4$ and $A = A^\star = 2.23219$.

parametrise the velocity distribution with another field, usually the flow rate $q = \int_0^h u\,\mathrm{d}y$ or the averaged velocity $\bar{u} = q/h$.

Following Ruyer-Quil *et al.* (2014), we decompose the streamwise velocity into a main part and a correction,

$$u = u^{(0)}(h, q) + \varepsilon u^{(1)}(h, q) \equiv h^2 g_0(\bar{y}) + \left(\frac{q}{h} - \frac{h^2}{3}\right) f_A(\bar{y}) + \varepsilon u^{(1)}(h, q), \tag{2.3}$$

where f_A refers to the ellipse-type velocity profile proposed by Usha *et al.* (2020):

$$f_A = K_p \left[\sqrt{A^2 - 4(\bar{y} - 1)^2} - B\right], \quad \text{with } K_p = \frac{1}{\frac{1}{4}A^2 \sin^{-1}(2/A) - \frac{1}{2}B}, \quad B = \sqrt{A^2 - 4}. \tag{2.4}$$

The ellipse velocity profile f_A and corrections $u^{(1)}$ fulfil the $O(\varepsilon)$ boundary conditions for the velocity and integral conditions:

$$\int_0^1 f_A(\bar{y})\,\mathrm{d}\bar{y} = 1, \quad f_A(0) = 0, \quad \frac{\mathrm{d}f_A}{\mathrm{d}\bar{y}}(1) = 0, \quad \int_0^h u^{(1)}(h, q)\,\mathrm{d}y = 0. \tag{2.5}$$

Consequently, (2.3) verifies $q = \int_0^h u\,\mathrm{d}y$ such that this decomposition is unique. Note that $u^{(0)}$ coincides with the Nusselt solution (2.2) for $q = h^3/3$, which corresponds to the in-depth integration of (2.2). The profile f_A involves only one free parameter A, which can be varied in the range $]2, \infty[$. In the limit $A \to 2$, f_A approaches a circular shape (see figure 1*a*). Note that, as A increases, the eccentricity of the ellipse approaches values closer to 1 (Usha *et al.* 2020), and f_A tends to a parabola as $A \to \infty$. The profiles for higher values of A ($= 5$, 10) are closer to each other and almost coalesce with the parabolic profile.

We retain the non-vanishing terms of highest order, namely first-order inertial terms and second-order viscous diffusion ones. Although second-order inertia terms can be retained, these terms may lead to non-physical behaviour, with the loss of solitary wave solutions,

https://doi.org/10.1017/jfm.2022.901 Published online by Cambridge University Press

as δ is raised (Ruyer-Quil *et al.* 2014):

$$\varepsilon u_{yy}^{(1)} = \varepsilon\delta(u_t^{(0)} + u^{(0)}\,u_x^{(0)} + v^{(0)}\,u_y^{(0)}) - b(h) - u_{yy}^{(0)} - \varepsilon^2\eta(2u_{xx}^{(0)} + [u_x^{(0)}|_{y=h}]_x) + O(\varepsilon^2), \tag{2.6a}$$

$$\varepsilon u^{(1)}|_{y=0} = 0, \quad \varepsilon u_y^{(1)}|_{y=h} = \varepsilon^2\eta(4h_x u_x^{(0)}|_{y=h} - v_x^{(0)}|_{y=h}) + O(\varepsilon^3). \tag{2.6b}$$

The resulting momentum balance (2.6*a*) is next averaged with a parabolic weight $w = g_0(\bar{y})$, the solution to $w_{yy} = \text{const.}$, since then

$$\int_0^h g_0 u_{yy}^{(1)}\,\mathrm{d}y = \tfrac{1}{2}u_y^{(1)}|_{y=h} - \int_0^h u^{(1)}\,\mathrm{d}y = \varepsilon\eta(2h_x u_x^{(0)}|_{y=h} - \tfrac{1}{2}v_x^{(0)}|_{y=h}). \tag{2.7}$$

As a result, the computation of the correction $u^{(1)}$, the solution to (2.6), is unnecessary to achieve consistency at order $O(\varepsilon)$. Since w is not proportional to $u^{(0)}$, the WRM differs here from the EIM – see Ruyer-Quil, Chakraborty & Dandapat (2012) and Samanta, Goyeau & Ruyer-Quil (2013) for other examples of the WRM approach where weight and test functions differ. The obtained averaged momentum balance thus reads

$$\delta q_t = \delta\left[\left(\frac{G}{S}\frac{q^2}{h^2} - \frac{G_1}{S}qh - \frac{G_2}{S}h^4\right)h_x - \left(\frac{F}{S}\frac{q}{h} + \frac{F_1}{S}h^2\right)q_x\right] + \frac{h}{3S}\left[b(h) - \frac{3q}{h^3}\right] + \eta\left[\left(\frac{J}{S}\frac{q}{h^2} - \frac{J_1}{S}h\right)h_x^2 - \frac{K}{S}\frac{q_x h_x}{h} - \left(\frac{L}{S}\frac{q}{h} + \frac{L_1}{S}h^2\right)h_{xx} + \frac{M}{S}q_{xx}\right], \tag{2.8}$$

where the ordering parameter ε has been dropped for simplicity. The coefficients F, G, etc. are functions of the parameter A, the expressions of which are given in Appendix A.

Compared to the RQM model derived by Ruyer-Quil & Manneville (2000), (2.8) contains deviatory terms that are not present there, corresponding to the coefficients G_1, G_2, F_1, J_1 and L_1. These terms arise due to the non-self-similar nature of $u_0(h, q)$ in the ansatz (2.3) as the parabolic profile $3g_0$ differs from the elliptic profile f_A. In the limit $A \to \infty, f_\infty = 3g_0$ and these terms vanish. Owing to these deviatory terms, the averaged momentum balance (2.8) differs from the expected form of an averaged momentum balance, akin to a viscous shallow-water equation (Gerbeau & Perthame 2001), where convective terms are quadratic with respect to the velocity, or equivalently the flow rate q, and viscous diffusion terms are linear with respect to q.

However, (2.8) can easily be rewritten in a form where convective terms are quadratic and diffusive terms are linear with respect to q by playing with the zeroth-order equivalence $q = h^3/3 + O(\varepsilon)$ to rewrite the inertia and diffusion terms while retaining consistency at $O(\varepsilon)$ for the former and $O(\varepsilon^2)$ for the latter. The result reads

$$\delta q_t = \delta\left[\left(\frac{G - 3G_1 - 9G_2}{S}\right)\frac{q^2}{h^2}h_x - \left(\frac{F + 3F_1}{S}\right)\frac{q}{h}q_x\right] + \frac{h}{3S}\left[b(h) - \frac{3q}{h^3}\right] + \eta\left[\left(\frac{J - 3J_1}{S}\right)\frac{q}{h^2}h_x^2 - \frac{K}{S}\frac{q_x h_x}{h} - \left(\frac{L + 3L_1}{S}\right)\frac{q}{h}h_{xx} + \frac{M}{S}q_{xx}\right]. \tag{2.9}$$

Completed by the (exact) mass balance $h_t + q_x = 0$, (2.8) or (2.9) form two-equation low-dimensional models, referred to as EVP and EVPM models, respectively. These models are consistent up to $O(\varepsilon)$ for inertial terms and up to $O(\varepsilon^2)$ for diffusive ones. As a consequence, the threshold of instability, $\delta_c = \frac{5}{2}\zeta$, is accurately captured by the

https://doi.org/10.1017/jfm.2022.901 Published online by Cambridge University Press

	$\frac{q^2}{h^2}h_x$	$\frac{q}{h}q_x$	$\frac{q}{h^2}h_x^2$	$\frac{h_xq_x}{h}$	$\frac{q}{h}h_{xx}$	q_{xx}	b
EVP ($A = A^\star$)	1.229	−2.329	3.761	−4.160	−5.656	4.471	0.853
EVPM ($A = A^\star$)	1.112	−2.347	3.574	−4.171	−5.738	4.471	0.853
EVPM ($A = 10$)	1.281	−2.426	3.985	−4.489	−5.992	4.499	0.833
RQM	1.285	−2.428	4	−4.5	−6	4.5	0.833

Table 1. Coefficients of (2.8) (EVP) and (2.9) (EVPM) compared with the RQM model (equation (14) in Ruyer-Quil *et al.* 2014).

two models. These two models lead to the same linear stability analysis of the Nusselt flat-film solution (same dispersion relation). Moreover, the locations of the marginal stability curves based on this dispersion relation (not shown) are nearly unaffected by the value of A for a wide range of parameters. This shows that the linear stability of the Nusselt film based on the EVP, EVPM and RQM models are nearly equivalent. Since the RQM model has been shown to accurately capture the solutions to the Orr–Sommerfeld problem (Ruyer-Quil & Manneville 2002), we conclude that our new formulations reproduce satisfactorily the primary instability of the film for all values of $A > 2$. The variations of the coefficients of the driving force (b), convective quadratic terms (q^2h_x/h, qq_x/h) and linear diffusive terms (qh_x^2/h^2, h_xq_x/h, qh_{xx}/h, q_{xx}) with respect to A are illustrated in table 1, which shows an excellent convergence to the RQM model as A is raised.

3. Results and discussion

The results from the EVP and EVPM models are obtained for a film over a vertical wall ($\beta = 90^\circ$) for typical values of the Kapitza number (water–glycerol solution, $Ka = 193$; plain water, $Ka = 3400$; and liquid nitrogen, $Ka = 10\,000$). We use the software AUTO07P (Doedel *et al.* 2007) to construct travelling-wave solutions, i.e. waves with a constant speed and shape, as solutions to a dynamical system in the three-dimensional phase space spanned by h, h' and h'', where the primes refer to the derivatives with respect to the coordinate $\xi = x - ct$ in a frame moving at the phase speed c. Notice that integration of the mass balance gives $q = ch + q_0$, where q_0 is a constant, which explains that the dynamic system is a function of h and its derivatives only. Solitary waves are computed in the limit of a large computational domain, through a homoclinic bifurcation. The procedure is detailed in Kalliadasis *et al.* (2012). The wave profile of a typical solitary wave, connecting the Nusselt film of thickness $h = 1$ to itself, is illustrated in figure 1(b). The maximum amplitude (h_{max}) and phase speed (c) of the one-hump solitary wave are displayed in figure 2 as a function of the reduced Reynolds number (δ) for different values of the parameter A. In the drag–gravity regime, at low values of δ, $c - 1$ and $h_{max} - 1$ are $\propto \delta^{3/2}$ (Ruyer-Quil & Kalliadasis 2012). Instead, at large values of δ, the phase speed c reaches a plateau for which the amplitude h_{max} continues to grow slowly, which corresponds to the drag–inertia regime.

Figure 2(a,c) shows how the adjustable parameter A affects the speed and amplitude of the waves. For $\delta \lessapprox 1$, all curves fall on a master curve. This is expected, since, in the drag–gravity regime, inertia is weak, viscosity is high and the wave dynamics is slaved to its kinematics so that the long-wave expansion holds accurately. Therefore, all models consistent with the long-wave expansion give very close results in that regime.

https://doi.org/10.1017/jfm.2022.901 Published online by Cambridge University Press

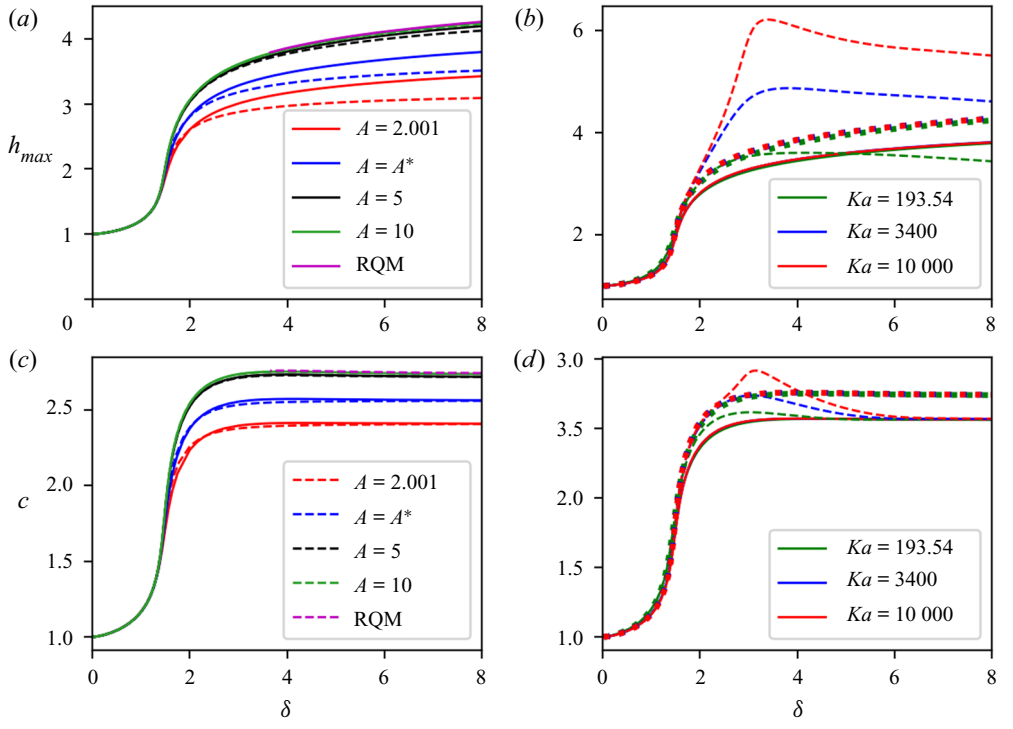

Figure 2. Characteristics of solitary waves: (*a*,*b*) amplitude h_{max}; (*c*,*d*) phase velocity c; (*a*,*c*) influence of varying A for $\eta = 0.01$; and (*b*,*d*) comparison to DNS on varying Ka for $A = A^\star = 2.23219$; for all panels, $\theta = 90^\circ$. In panels (*a*,*c*) dashed lines are for (2.8) (EVP) and solid lines are for (2.9) (EVPM). In panels (*b*,*d*) solid lines are for (2.9) (EVPM), dotted lines are for RQM model, and dashed lines are for DNS (Chakraborty *et al.* 2014).

However, for $\delta \gtrapprox 1$, inertia is dominant and the influence of A is significant. The asymptotic speed $\lim_{\delta\to\infty} c \equiv c_\infty$ increases with A and reaches a maximum as the EVP and EVPM models converge to the RQM model ($c_\infty \approx 2.738$). The EVPM model systematically predicts larger wave amplitudes than the EVP model.

Ruyer-Quil & Manneville (2005) have shown that the asymptotic speed c_∞ is obtained when the second fixed point location $h_{II} = -1/2 + \sqrt{3(c - 1/4)}$, at which gravity and viscous drag compensate each other (i.e. $q = h^3/3$), corresponds to the critical level at which inertia terms cancel out, which gives

$$c^2 + \left(\frac{G - 3G_1 - 9G_2}{S}\right)\frac{h_{II}^4}{9} - c\left(\frac{F + 3F_1}{S}\right)\frac{h_{II}^2}{3} = 0 \tag{3.1}$$

for both (2.8) and (2.9). Adjusting c_∞ to its prediction 2.560 found by DNS gives $A = A^\star \approx 2.23219$. The DNS results obtained by Chakraborty *et al.* (2014), along with the solutions to RQM model and to EVPM for $A = A^\star$, are presented for different Kapitza numbers in figure 2(*b*,*d*). Results from the EVP model, which somewhat underestimate the amplitude of solitary waves, are not shown. The choice of $A = A^\star$ for comparison is dictated by the requirement that the asymptotic speed c_∞ of the models matches the predictions of DNS. Note that the dependence of the amplitude of the DNS results on the Kapitza number is an effect of the complex velocity distribution (departure from parabolic profile) under the capillary ripples. With two-equation models, such as EVP or EVPM

https://doi.org/10.1017/jfm.2022.901 Published online by Cambridge University Press

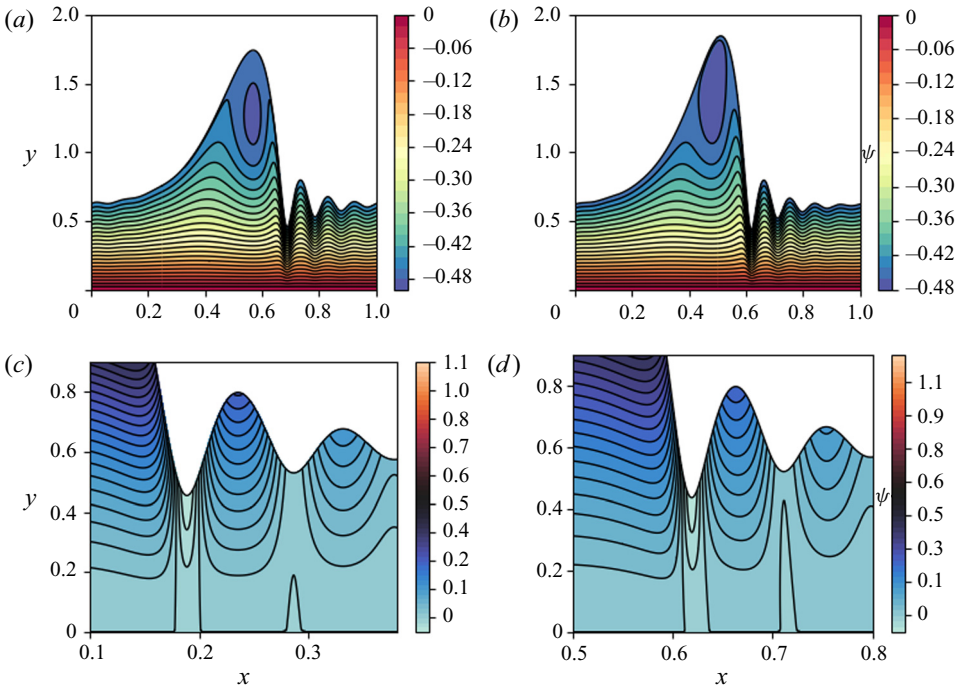

Figure 3. Streamlines in the laboratory and moving frames of a travelling-wave solution to (2.9) (EVPM) with $A = A^\star$ corresponding to an experiment by Dietze, Al-Sibai & Kneer (2009): vertical wall, water–dimethyl sulfoxide (DMSO) mixture, $Re = 15$, $f = 16$ Hz, $\mu = 3.13 \times 10^{-3}$ Pa s, $\rho = 1098.3$ kg m^{-3} and $\sigma = 0.0484$ N m^{-1} ($\delta = 14.21$, $\zeta = 0$, $\eta = 0.0876$ and $Ka = 509.5$). (*a*) Equation (2.9) (EVPM), moving frame; (*b*) DNS, moving frame; (*c*) equation (2.9) (EVPM), laboratory frame; and (*d*) DNS, laboratory frame.

models, there is no dependence of wave amplitude on the Kapitza number (no effect of capillarity on amplitude) and a monotonic behaviour of speed and amplitude with respect to the reduced Reynolds number δ is observed.

The performance of the EVPM model is further assessed by comparing its predictions to DNS for a large-amplitude travelling wave corresponding to an experiment performed by Dietze *et al.* (2009) in the drag–inertia regime ($\delta = 14.21$, $Ka = 509.5$). The DNS travelling-wave solution has been obtained by a projection method on Chebyshev polynomials and continuation method (see Cellier & Ruyer-Quil (2020) for details). Figure 3(*a*) displays the wave profiles and streamlines in the moving frame computed from the modified model. The streamfunctions have been computed from the zeroth-order velocity distribution $u^{(0)}(h, q)$, as adding the correction $u^{(1)}$ reduces the agreement with DNS whenever the long-wave expansion does not strictly hold, as is the case for large-amplitude solitary waves (Ruyer-Quil *et al.* 2014).

The comparison with the DNS results is quite satisfactory, as evidenced by the predictions regarding the intensity and location of the recirculation zone in the main hump. The accumulation of capillary ripples at the foot of the solitary wave is well captured by the modified model (cf. figure 3*c*) and is in striking agreement with the corresponding DNS results (figure 3*d*). Streamlines in the laboratory frame (figure 3*c*,*d*) reveal the onset of back-flows, or separation eddies, at the locations of troughs in the capillary ripples preceding the main hump. Once again, the EVPM model captures remarkably well the

https://doi.org/10.1017/jfm.2022.901 Published online by Cambridge University Press

flow pattern predicted by DNS, which shows that the EVP velocity profile $u^{(0)}$ given by (2.3) is a satisfactory approximation of the true velocity profile.

4. Concluding remarks

Based on a combination of a parabolic and an ellipse profile introduced by Usha *et al.* (2020), we have derived a new low-dimensional two-equation model for thin-film flows using the WRM. The model is first-order consistent for inertia terms and second-order consistent for diffusive terms, which guarantees that it captures the primary instability adequately. Equation (2.9) presents the usual structure for a shallow-water momentum balance, where convective terms are quadratic with respect to the flow rate q and diffusive terms are linear in q. The EVPM (2.9) successfully and satisfactorily captures the nonlinear wave properties of film flows down a vertical wall, in both the drag–gravity and drag–inertia regimes, such as asymptotic wave speed, maximum wave height, wave profiles, streamlines in the moving frame and the flow patterns in the laboratory frame. In particular, it is able to capture the onset of closed separation vortices which can form underneath the troughs of precursory capillary ripples (Dietze *et al.* 2009).

This study is another step forward in the modelling of falling thin-film flows, thereby offering new perspectives for theoretical and applied investigations. This calls for further in-depth investigation of the EVPM model and similar formulations, taking full advantage of the adjustable ansatz for the velocity profile.

Acknowledgements. The authors thank S. Chakraborty, P.-K. Nguyen and V. Bontozoglou for providing them with the DNS results shown in figure 2.

Funding. C.R.-Q. acknowledges support from FRAISE project ANR-16-CE06-0011 of the French National Research Agency. S.M. thanks the Vellore Institute of Technology, Vellore, for providing the VIT SSEED Grant - RGEMS Fund (SG20220087) for carrying out this research work.

Declaration of interests. The authors report no conflict of interest.

Author ORCIDs.
Sanghasri Mukhopadhyay https://orcid.org/0000-0001-5360-1190;
Christian Ruyer-Quil https://orcid.org/0000-0002-7717-5015;
R. Usha https://orcid.org/0000-0002-8026-6399.

Appendix A. Coefficients of EVP (2.8) and EVPM (2.9) models

$$S = \frac{16B + 48N - 3A^2N}{96N}, \tag{A1}$$

$$F = \frac{-16(816 - 760A^2 + 75A^4)B + 30A^2(736 - 252A^2 + 17A^4)C + 45A^6BC^2}{720BN^2}, \tag{A2}$$

$$F_1 = \frac{1}{138240N^2}[43008 + 405A^8C^2 + 128A^2(-3317 + 816BC) - 180A^6(-9 + 9BC + 76C^2) + 240A^4(131 + 35BC + 312C^2)], \tag{A3}$$

$$G = \frac{(-576 + 520A^2 - 30A^4)B + 15A^2(64 - 20A^2 + A^4)C}{60BN^2}, \tag{A4}$$

https://doi.org/10.1017/jfm.2022.901 Published online by Cambridge University Press

$$G_1 = \frac{1}{11520N^2}[9216 + 896A^2(-82 + 21BC) + 15A^4(496 + 36A^2 + 4(4 - 9A^2)BC + 3(-8 + A^2)(-32 + 3A^2)C^2)], \tag{A5}$$

$$G_2 = -\frac{1}{46080N^2}[6144 + 315A^8C^2 + 128A^2(-779 + 176BC) - 60A^6(-21 + 21BC + 92C^2) + 48A^4(65 + 145BC + 488C^2)], \tag{A6}$$

$$J = \frac{1}{24BN^3}[-8(56 + 13A^2)B^4 - 3A^6(16 + A^2)BC^3 + 128AB^3R + 4A^2B^2C((64 + 23A^2)B - 32AR) + 2A^4C^2(-160 + 68A^2 - 7A^4 + 16ABR)], \tag{A7}$$

$$J_1 = -\frac{1}{36BN^3}[4A^2B^2(16B + A(-64 + 64A^2 - 19AB))C + 15A^8BC^3 + 8B^2(32 - 76A^2 + 17A^4 - 32ABV) - 2A^4C^2(-32 - 44A^2 + 13A^4 + 32ABV)], \tag{A8}$$

$$K = \frac{1}{12(16 - 4A^2 + A^4C^2)}[512 + 4A(40B + A(-52 + 5A^2 - 8AB)) + A^2C(-64B + 16A(5 + A(-A + B)) + 3A^4C)], \tag{A9}$$

$$L = \frac{1}{24N^3}[4A^2B(160B + A(-176 + 16A^2 - 7AB))C - 2A^4(80B + A(-88 + A(8A + B)))C^2 + 3A^8C^3 + 8B^2(5BQ - 8AT)], \tag{A10}$$

$$L_1 = \frac{1}{144N^3}[-640AB^2 + 160A^2B^2C + 32A^7C^2 - 15A^8C^3 + 128A^3B(B + 5C) - 32A^5C(4B + 5C) + 2A^6C^2(29B + 36C) - 4A^4BC(13B + 64C) - 8B^3Q], \tag{A11}$$

$$M = \frac{-48B + 72N + A(64 - 3AN)}{48N}, \tag{A12}$$

where $B = \sqrt{A^2 - 4}$, $C = \arctan(2/B)$, $N = (A^2C - 2B)$, $R = A^2 + 5$, $V = A^2 - 1$, $T = A^2 - 11$ and $Q = A^2 - 16$.

References

Cellier, N. & Ruyer-Quil, C. 2020 A new family of reduced models for non-isothermal falling films. *Intl J. Heat Mass Transfer* **154**, 119700.

Chakraborty, S., Nguyen, P.-K., Ruyer-Quil, C. & Bontozoglou, V. 2014 Extreme solitary waves on falling liquid films. *J. Fluid Mech.* **745**, 564–591.

Dietze, G.F., Al-Sibai, F. & Kneer, R. 2009 Experimental study of flow separation in laminar falling liquid films. *J. Fluid Mech.* **637**, 73–104.

Doedel, E.J., Champneys, A.R., Fairgrieve, T.F., Kuznetsov, Y.A., Sandstede, B. & Wang, X. 2007 AUTO-07p: Continuation and Bifurcation Software for Ordinary Differential Equations (with HomCont). Available at https://sourceforge.net/projects/auto-07p/.

Gerbeau, J.-F. & Perthame, B. 2001 Derivation of viscous Saint-Venant system for laminar shallow water; numerical validation. *Discrete Continuous Dyn. Syst.* B **1** (1), 89–102.

Han, Y. & Rogers, R.J. 1996 Squeeze film force modeling for large amplitude motion using an elliptical velocity profile. *J. Tribol.* **118** (3), 687–692.

https://doi.org/10.1017/jfm.2022.901 Published online by Cambridge University Press

KALLIADASIS, S., RUYER-QUIL, C., SCHEID, B. & VELARDE, M.G. 2012 *Falling Liquid Films*. Applied Mathematical Sciences, vol. 176. Springer.

NOBLE, P. & VILA, J.P. 2013 Thin power-law film flow down an inclined plane: consistent shallow-water models and stability under large-scale perturbations. *J. Fluid Mech.* **735**, 29–60.

OOSHIDA, T. 1999 Surface equation of falling film flows which is valid even far beyond the criticality. *Phys. Fluids* **11**, 3247–3269.

RICHARD, G.L., GISCLON, M., RUYER-QUIL, C. & VILA, J.P. 2019 Optimization of consistent two-equation models for thin film flows. *Eur. J. Mech. B/Fluids* **76**, 7–25.

RICHARD, G.L., RUYER-QUIL, C. & VILA, J.P. 2016 A three-equation model for thin films down an inclined plane. *J. Fluid Mech.* **804**, 162–200.

RUYER-QUIL, C., CHAKRABORTY, S. & DANDAPAT, B.S. 2012 Wavy regime of a power-law film flow. *J. Fluid Mech.* **692**, 220–256.

RUYER-QUIL, C. & KALLIADASIS, S. 2012 Wavy regimes of film flow down a fiber. *Phys. Rev.* E **85**, 046302.

RUYER-QUIL, C., KOFMAN, N., CHASSEUR, D. & MERGUI, S. 2014 Dynamics of falling liquid films. *Eur. Phys. J.* E **37** (4), 30.

RUYER-QUIL, C. & MANNEVILLE, P. 2000 Improved modeling of flows down inclined planes. *Eur. Phys. J.* B **15** (2), 357–369.

RUYER-QUIL, C. & MANNEVILLE, P. 2002 Further accuracy and convergence results on the modeling of flows down inclined planes by weighted-residual approximations. *Phys. Fluids* **14** (1), 170–183.

RUYER-QUIL, C. & MANNEVILLE, P. 2005 On the speed of solitary waves running down a vertical wall. *J. Fluid Mech.* **531**, 181–190.

SAMANTA, A., GOYEAU, B. & RUYER-QUIL, C. 2013 A falling film on a porous medium. *J. Fluid Mech.* **716**, 414–444.

USHA, R., CHATTOPADHYAY, G. & TIWARI, N. 2020 Evolution of a thin film down an incline: a new perspective. *Phys. Fluids* **32** (1), 013603.

https://doi.org/10.1017/jfm.2022.901 Published online by Cambridge University Press